### Title

Numerical Modeling of Deep Borehole Heat Exchanger in Southern California - Feasibility Study




### Authors

Chen, Haohua
Tomac, Ingrid



### Publication Date

2023-06-25

### DOI

10.56952/arma-2023-0582

Peer reviewed

ARMA 23–0582

# Numerical Modeling of Deep Borehole Heat Exchanger in Southern California - Feasibility Study

Chen, Haohua

*Department of Structural Engineering, University of California San Diego, La Jolla, CA 92093-0085, United States*

Tomac, Ingrid

*Department of Structural Engineering, University of California San Diego, La Jolla, CA 92093-0085, United States*



This paper was prepared for presentation at the 57th US Rock Mechanics/Geomechanics Symposium held in Atlanta, Georgia, USA, 25-28 June 2023. This paper was selected for presentation at the symposium by an ARMA Technical Program Committee based on a technical and critical review of the paper by a minimum of two technical reviewers. The material, as presented, does not necessarily reflect any position of ARMA, its officers, or members. Electronic reproduction, distribution, or storage of any part of this paper for commercial purposes without the written consent of ARMA is prohibited. Permission to reproduce in print is restricted to an abstract of not more than 200 words; illustrations may not be copied. The abstract must contain conspicuous acknowledgement of where and by whom the paper was presented.

**ABSTRACT:** This paper presents an investigation into the feasibility of low thermal-gradient deep Borehole Heat Exchanger (BHE) applications on campus at the University of California San Diego (UCSD). With a review of primary source data for various formations and well logs around the UCSD campus, the stratigraphy and thermo-physical properties of the formation were evaluated. Based on the collected information, a numerical model for the BHE application was developed. Circulation of water through a closed coaxial loop system considers the variation of several parameters in order to develop the feasibility study and obtain guidelines for the future UCSD geothermal resource. For example, multiple layers of the formation and thus the variance of ground thermal conductivities along the vertical direction were considered, and fluid velocity and borehole depth were varied. To do that, a numerical scheme that employs finite element schemes for modeling Navier-Stokes fluid flow and heat flow and transport in the BHE system constructed the numerical model. The numerical model verification was first performed via comparisons with a field test on BHE from the literature. Then the effects of the thermal properties, volumetric flow rate, and other relevant parameters were systematically analyzed by using the developed numerical modeling. The proposed model can be used to evaluate the suitability of BHE applications with low thermal-gradient in southern California.

## 1. INTRODUCTION

The utilization of fossil fuels has surged significantly during the last half-century, resulting in enormous carbon dioxide (CO2) emissions and thus significant climate change. To tackle that, the United Nations, the G7 economies and many countries around the world have started or are going to promote the shift to renewable energy (UN DESA 2017; Gielen et al. 2019; G7 2021). Among different renewable energy, geothermal energy has been used for centuries and it is expected to meet 3%-5% of global demand by 2050 (Craig and Gavin 2018). Based on the depth of geothermal energy reservoirs, there are two major types of geothermal systems: shallow geothermal systems (≤400 m) and deep geothermal systems (> 400 m) according to White (1966).

Different exploration strategies have been developed for extracting heat from deep geothermal reservoirs, such as Enhanced Geothermal Systems (EGS) and Borehole Heat Exchangers (BHE). In an EGS, fluid is injected to re-open pre-existing fractures and thus increase the permeability of rock. Then the cold fluid can circulate throughout fractured hot rock and be used to generate energy after being pumped out to the ground surface at higher temperatures (Tester et al. 2006). However, the drilling costs of the EGS can be 42%-95% of the total cost (Tester et al. 1994). Therefore, attention has also been paid to extending pre-drilled and abandoned wells for geothermal energy applications. On the other hand, U-shaped and coaxial BHE extract geothermal energy from the ground with no direct contact between the fluid and hot rock/soil. Due to the cost and difficulty of drilling U-shaped wells, the coaxial borehole is considered more reliable and feasible (He et al. 2021). According to previous studies (Caulk and Tomac 2017; Kharseh et al. 2019; Hu et al. 2019), oil and gas wells could be transformed as coaxial BHE. Besides, there are approximately 147127 abandoned, plugged, and/or inactive wells according to the California Department of Conservation, Division of Oil and Gas and Geothermal Resources. In this regard, there is a need to study the feasibility of BHE using abandoned wells in southern California.

Field tests and numerical simulations have been performed to investigate the performance, optimization,

and application of BHE. For instance, field tests on the short-term behavior of BHEs have been conducted in Hawaii (Morita et al. 1992), Qingdao, China (Bu et al. 2019), and Beppu, Japan (Pokhrel et al. 2022). Besides, numerical simulations (Shi et al. 2019; Iry and Rafee 2019; Wang et al. 2022) using different software such as COMSOL Multiphysics (COMSOL 2022), ANSYS FLUENT (ANSYS 2016), and FEFLOW (Diersch 2014) have been adopted to analyze the performance of coaxial BHE using different working fluids and under different geological conditions. Both field tests and numerical simulations contribute to the analyses of BHE using different techniques and provide important insight for the feasibility studies of BHE in different geological conditions.

In this study, an investigation into the feasibility of low thermal-gradient deep Borehole Heat Exchanger (BHE) applications on campus at the University of California San Diego (UCSD) is presented. With a review of primary source data for various formations and well logs around the UCSD campus, the stratigraphy and thermo-physical properties of the formation were evaluated. Based on the collected information, a numerical model for the BHE application was developed. The circulation of water through a closed coaxial loop system considers the variation of several parameters in order to develop the feasibility study and obtain guidelines for the future UCSD geothermal resource. The verification of the numerical model with a field test was performed and parametric studies were conducted on the fluid rate, borehole depth and other properties using the well-calibrated model.

## 2. SITE CONDITIONS

The intended site for geothermal investigation is located at the Central Facilities Plant at the University of California, San Diego. A plan view of the site is shown in Fig. 1. There are several well logs available near the site. Among them, the nearest plugged dry hole Capital well No. 1 with lithology log to 5860 ft below the ground surface is 5.6 km away from the site. And the nearest USGS monitoring well SDAQ with well log to 950 ft below the ground surface is about 15 km from the site. Generally, geology consists of shallow sandy soils (up to around 230 m), then shale and conglomerate were encountered below 230 m and sedimentary rocks such as limestone can be seen at a deeper depth (> 630 m). The detailed layers of the ground are given later.

### *2.1. Physical properties of rock*

The two aforementioned boreholes lithology descriptions and log SDAQ's log measurements provide data and information for indirect determination of the formation's thermal conductivity $\lambda$ and the specific heat capacity $C_p$ at different depths, which were not measured directly on the site to date. The updated ground thermal property table by Dalla Santa et al. (2020) provides the $\lambda$ and $C_p$ from lithology as summarized in Table 1 (Dalla Santa et al. 2020).

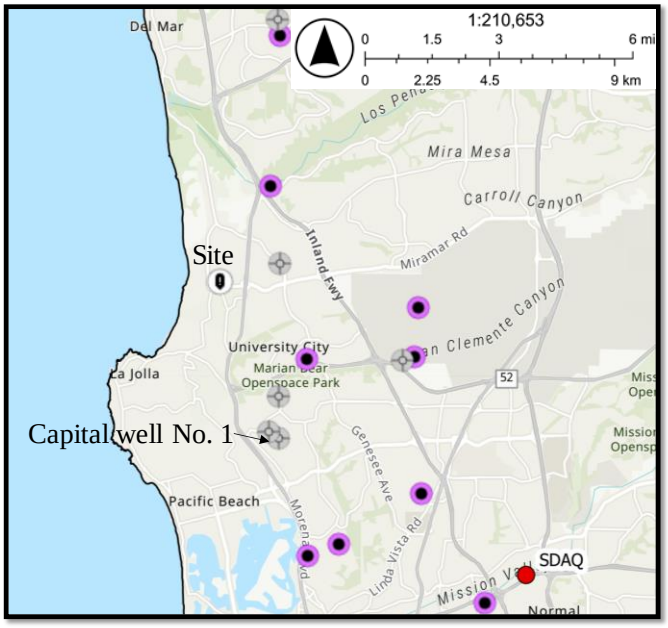


Fig. 1 Plan view of the site location within the San Diego metropolitan area.

Table 1 Physical properties estimated from lithology.

| Material | $\lambda$ (W/m/K) | $C_p$ (J/kg/K) |
|---|---|---|
| Conglomerate | 1.5-5.1 (1.94[a]) | 667-1182[b] |
| Sandstone | 0.72-6.5 (2.6) | 774-938 |
| Clay-mudstone | 0.59-3.48 (2.13) | 667-826 |
| Shale | 0.55-4.25 (2.07) | 600-1200 |
| Limestone | 0.6-5.1 (2.5) | 646-944 |
| Gravel with sand, wet | 0.2-3 (1.08) | 700-900 |
| Medium sand, wet | 1-2.6 (1.9) | 604-874 |
| Silty sand/ sandy silt, wet | 1.2-2.25 (1.62) | 698-936 |
| Silt and clayey silt, wet | 0.82-2.6 (1.45) | 694-917 |
| Plastic clay, wet | 0.6-1.9 (1.1) | 234-1007 |

Note: [a] is the representative value, [b] takes the average value as the representative value (revised from Dalla Santa et al. 2020).

USGS provides the well log, temperature gradient, natural gamma, spontaneous potential, resistivity, electromagnetic conductivity, and sonic velocity up to 790 m below the ground surface, and the formation mainly consists of sandy soils within the drilled depth of the wells (USGS 2023). According to Hartmann et al. (2005), the $\lambda$ of saturated sandy soil can be generally estimated from correlations to sonic velocity $v_p$ following the relationship:

$$\lambda = (0.372 \pm 0.035)v_p + 1.809 \pm 0.118 \quad (1)$$

where $\lambda$ is in the unit of W/(m·K) and $v_p$ is in km/s. Since the lithology from SDAQ is mainly sandy soil, Eq. (2) is used to determine the ranges of $\lambda$.

Based on Table 1 and Eq. (2), the thickness of major layers is evaluated based on value ranges of $\lambda$ and $C_p$ and the properties at different depths weighted averages:

$$p_{ave} = \frac{\sum p_i t_i}{\sum t_i} \quad (2)$$

where $p_{ave}$ is the average property of one specific layer, $p_i$ is the property of a specific depth with a thickness of $t_i$, $t_i$ is the thickness of formation between two adjacent measurements from the borehole. Since Table 1 and Eq. (1) provide lower and upper bound values for $\lambda$ and $C_p$ at different depths, the lower and upper bounds for a specific layer are estimated from the corresponding lower and upper bound values from different depths using Eq. (2).

As a result, the formation is generally classified as eight layers as shown in Table 2. It should be noted that the thickness of layer 8 shown in Table 2 is only to the bottom of capital well No. 1, which is 1868 m below the ground surface. If the simulated BHE is deeper than 1868 m, layer 8 is extended to the bottom of the model for conservative consideration.

Table 2 Physical properties of different layers at UCSD site

| Layer # | Features | Thickness (m) | λ (W/m/K) | Cp (J/kg/K) |
|---|---|---|---|---|
| 1 | Silt and sand | 15.2 | 2-2.48 (2.24[a]) | 694-917[b] |
| 2 | Sand to gravelly sandy silt | 45.7 | 2.05-2.53 (2.29) | 630-886 |
| 3 | Sandy silt and silty sand | 225.6 | 2.32-2.86 (2.59) | 693-922 |
| 4 | Shale, lime, and sand | 120.4 | 0.96-4.25 (2.03) | 633-1093 |
| 5 | Shale | 203.9 | 0.55-4.25 (2.07) | 600-1200 |
| 6 | Conglomerate | 129.2 | 1.04-3.04 (1.92) | 612-930 |
| 7 | Mostly shale | 496.8 | 0.56-4.24 (2.07) | 600-1197 |
| 8 | Limestone | 631.5[c] | 0.67-5 (2.28) | 662-1063 |

Note: [a] is the representative value, [b] takes the average value as the representative value, [c] is the depth of layer 8 to the bottom of capital well No. 1 (1868 m below ground surface).

### 2.2. *Temperature gradient*

As mentioned before, the temperature gradient was measured by USGS well log, generally falling between 15 to 60 °C/km according to USGS (2023). The nearest measured temperature profile is SDAQ as shown in Fig. 2. And the average temperature gradient of SDAQ is 32.8 °C/km. To be conservative, the temperature gradient is assumed as 30 °C/km in the numerical model.

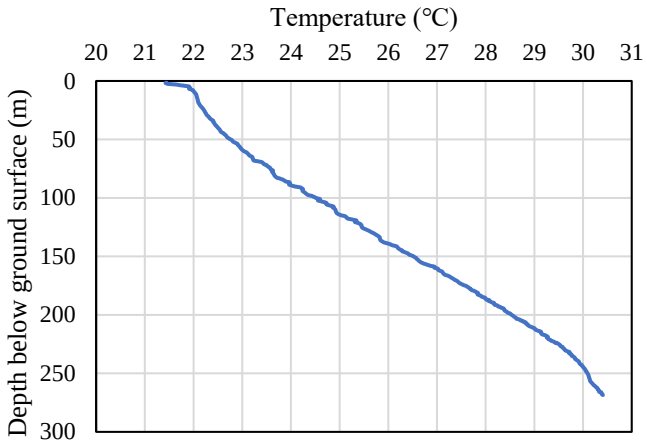


Fig. 2 Temperature profile of formation at SDAQ

## 3. METHODOLOGY

A numerical simulation is constructed to solve the fluid flow and heat transport of the BHE in the UCSD campus by using COMSOL Multiphysics software (COMSOL 2022). The model considers both convective and conductive heat transfer between the incompressible working fluid and the surrounding formation matrix. The governing Navier-Stokes equation of the fluid inside the coaxial BHE is:

$$\rho_f \frac{\partial \boldsymbol{u_f}}{\partial t} + \rho_f (\boldsymbol{u_f} \cdot \nabla)\, \boldsymbol{u_f} = \nabla \cdot (-p_f \boldsymbol{I} + \boldsymbol{K}) + \rho_f g \quad (3)$$

$$\boldsymbol{K} = (\mu + \mu_T)\left[\nabla \boldsymbol{u_f} + (\nabla \boldsymbol{u_f})^T\right] \quad (4)$$

where $\rho_f$ is the density of fluid, $\boldsymbol{u_f}$ is the velocity vector of fluid, $p_f$ is the fluid pressure, $\mu$ is the dynamic viscosity of fluid, $\mu_T$ is the Eddy viscosity that is a function of the local flow conditions, and it reduces to zero if the flow is laminar.

In this study, the k-ε turbulence model proposed by Launder and Spalding (1974) is utilized to determine $\mu_T$

$$\mu_T = \rho_f C_\mu \frac{k^2}{\varepsilon} \quad (5)$$

where $C_\mu = 0.09$ is a constant, $k$ is the turbulent kinetic energy, $\varepsilon$ is the rate of dissipation of turbulent kinetic energy. $k$ and $\varepsilon$ are determined by solving:

$$\rho_f (\boldsymbol{u_f} \cdot \nabla) k = \nabla \cdot \left[\left(\mu + \frac{\mu_T}{\sigma_k}\right)\nabla k\right] + p_k - \rho_f \varepsilon \quad (6a)$$

$$\rho_f (\boldsymbol{u_f} \cdot \nabla) \varepsilon = \nabla \cdot \left[\left(\mu + \frac{\mu_T}{\sigma_\varepsilon}\right)\nabla \varepsilon\right] + C_{1\varepsilon}\frac{\varepsilon}{k} p_k - C_{2\varepsilon}\rho_f \frac{\varepsilon^2}{k} \quad (6b)$$

$$p_k = \mu_T \left\{\nabla \boldsymbol{u_f} : \left[\nabla \boldsymbol{u_f} + (\nabla \boldsymbol{u_f})^T\right]\right\} \quad (6c)$$

where $\sigma_k = 1.00$ is a constant, $\sigma_\varepsilon = 1.30$ is a constant, $C_{1\varepsilon} = 1.44$ and $C_{2\varepsilon} = 1.92$,

And conservation of fluid mass can be expressed as

$$\rho_f \nabla \cdot \boldsymbol{u_f} = \mathbf{0} \quad (7)$$

To consider the heat convection and conduction within the formation, the conservation of energy equation is

$$\rho_g C_{pg} \frac{\partial T_g}{\partial t} + \rho_g C_{pg} \boldsymbol{u_g} \cdot \nabla T_g = \nabla \cdot (\lambda_g \nabla T_g) + Q_g \quad (8)$$

where $\rho_g$ is the density of ground formation, $C_{pg}$ is the specific heat capacity of the ground, $\boldsymbol{u_g}$ is the velocity vector of the ground, $T_g$ is the temperature of ground formation, $\lambda_g$ is the thermal conductivity of the ground, $Q_g$ is the additional heat source of ground formation. Note that $\boldsymbol{u_g}$ is taken as zero for simplicity, where the heat conduction dominates over convection within the ground formation, because the BHE system is isolated.

Similarly, the conservation of energy equation of fluid can be expressed as:

$$\rho_f C_{pf} \frac{\partial T_f}{\partial t} + \rho_f C_{pf} \boldsymbol{u_f} \cdot \nabla T_f = \nabla \cdot (\lambda_f \nabla T_f) \quad (9)$$

where $C_{pf}$ is the specific heat capacity of fluid, $T_f$ is the temperature of fluid, $\lambda_f$ is the thermal conductivity of fluid.

The thermal power of the coaxial BHE $Q_{out}$ can be expressed as

$$Q_{out} = C_{pf} q (T_{out} - T_{in}) \quad (10)$$

where $q$ is the volumetric flow rate of fluid through the BHE, $T_{out}$ and $T_{in}$ is the outlet and inlet temperature of the fluid within the coaxial BHE.

The geometry of the BHE and ground formation are shown in Fig. 3. Due to the symmetry of the coaxial BHE, a 2D axisymmetric model is built. To eliminate the effects of the boundary, the depth of the domain $d_d$ is set to be 200 m deeper than the BHE and the radius of the domain $r_d$ is 80 m. To well represent the velocity profile of the flow, the cross-sections of the inlet and outlet of the BHE are discretized into 6 elements. And the maximum length of the elements of the fluid along the depth direction is set to be 0.1 m. And the total number of elements of the models ranges from 190000 to 830000 based on different BHE lengths.

## 4. MODEL VALIDATION

In this section, the established model is validated by field test data from the island of Hawaii by Morita (1992) on an 879.6 m deep BHE. The outer pipe of the BHE was a K-55 casing with a $\lambda$ of 40 W/(m·K) and a $C_p$ of 1900 J/(kg·K), and the insulated inner pipe has a $\lambda$ of 0.06 W/(m·K). Along the whole depth of the BHE, the pipe outer diameter, outer pipe inner diameter, inner pipe outer diameter, and inner pipe inner diameter were 17.78 cm, 16.17 cm, 8.89 cm, and 5.06 cm, respectively. Water at a fixed temperate of 30°C was used as the working fluid and injected from the annulus at a constant flow rate of 4.8 $m^3$/h (80 l/min). Fig. 4 shows the temperature profile of the ground from Morita et al. (1992). The $\lambda$ and $C_p$ of the formation determined from the field test were 1.6 J/(kg·K) and 870 W/(m·K).

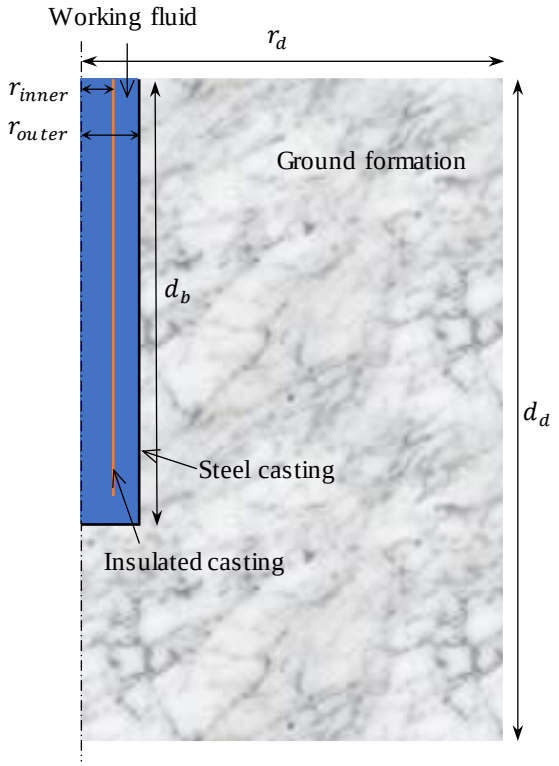


Fig. 3 Geometry of the BHE and ground formation.

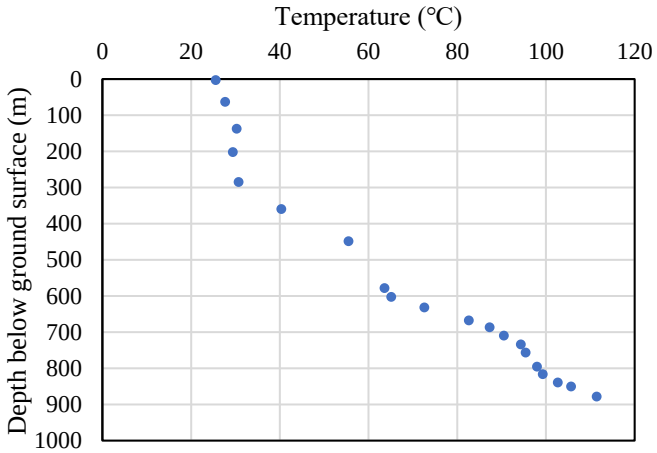


Fig. 4 Temperature profile of field test from Hawaii (revised from Morita 1992).

Fig. 5 shows the outlet water temperature versus time from the field test and the simulation by this study. As can be seen, within 12 h, the simulation generally agrees with the field test, except that the simulated temperature peak is delayed a little bit compared to the field test. This is probably because the transient model cannot well capture the onset of circulation of water under real

conditions and the little fluctuation of water temperature as shown in Fig. 5a. As for the temperature evolution in 7d in Fig. 5b, the simulation is in good agreement with the field test. Therefore, the proposed simulation model can well capture the behavior of coaxial BHE with time.

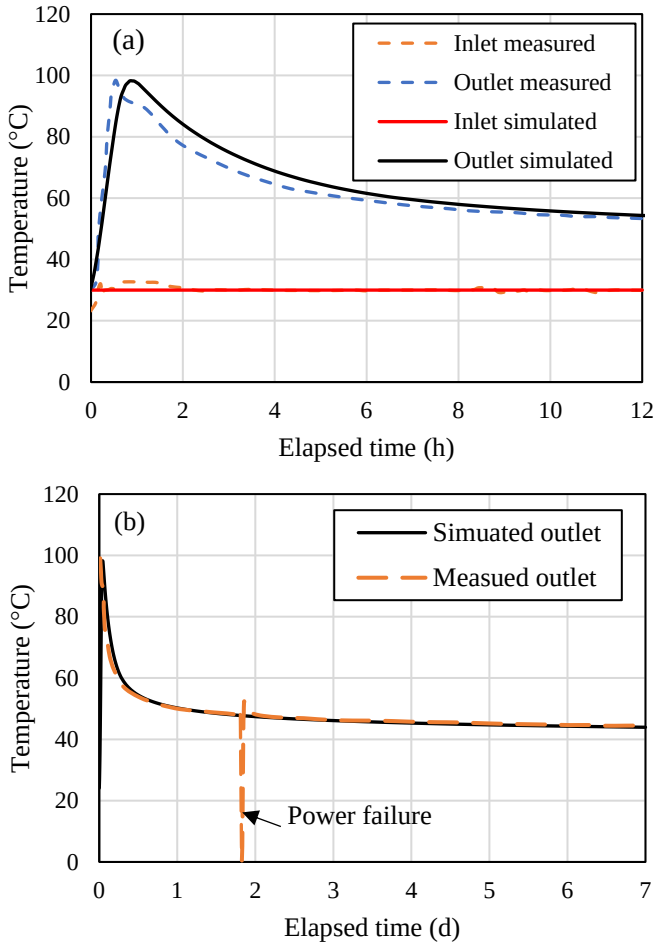


Fig. 5 Comparison between field test (Morita 1992) and simulation: (a) within 12 h; and (b) within 7 d.

## 5. PARAMETRIC STUDIES

In this section, the ground formation from the UCSD site in section 2 is adopted in the numerical modeling. Table 3 summarizes the geometry and thermal properties of the BHE.

Table. 3 Properties of BHE at UCSD site.

| $r_{inner}$ (mm) | $r_{outer}$ mm) | Thickness of pipe (mm) | | λ (W/m/K) | | Cp (J/kg/K) | | Depth $d_b$ (km) |
|---|---|---|---|---|---|---|---|---|
| | | Inner | Outer | Inner | Outer | Inner | Outer | |
| 56.90 | 80.49 | 10.45 | 8.05 | 0.05 | 44 | 300 | 475 | 1-4 |

Table 2 provides the physical properties of the ground formation on site, and the representative values are used if not specifically stated. The inlet water pressure is set to be 14°C according to the average temperature at San Diego during the winter season. In the following, parametric studies are performed on the effects of formation properties, BHE length (1-4 km), and flow rate (5-20 $m^3$/h) on the behavior of the coaxial BHE by using the proposed simulation models.

### 5.1. *Effect of formation properties*

Fig. 6 investigates the evolution of outlet fluid temperature with time by using different formation properties, i.e. lower bound, upper bound, and representative values, as listed in Table 2. Generally, the outlet fluid temperature surges to its peak value in a short time (less than 12 hours) and then significantly decreases in 1 day, and then gradually decreases during the operation with different formation properties and BHE lengths. And the outlet temperature barely changes after operating for 5 years. As expected, the outlet temperature is higher with the higher thermal conductivities of the formation at different time. Since the relation of outlet fluid temperature and time is similar for different cases, the plots of outlet temperature versus time are skipped in the following sections to avoid redundancy.

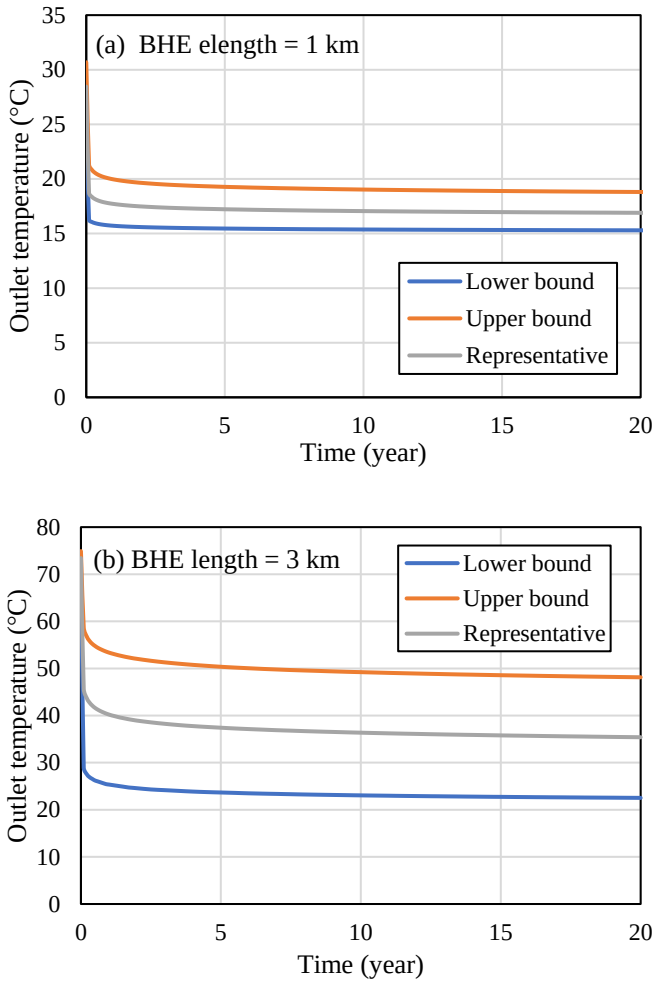


Fig. 6 Relation between outlet fluid temperature and operation time with different formation properties at a flow rate of 10 $m^3$/h: (a) BHE length of 1 km; and (b) BHE length of 3 km

Since the long-term performance of BHE is the major concern of the feasibility study, Fig. 7 shows the effect

of formation properties on the outlet fluid temperature and thermal power of the BHE after operation for 20 years. As can be seen, higher outlet temperature and thermal power can be obtained if higher thermal conductivities and specific heat capacities are considered. And the effect of formation properties increases with the BHE length. This is because the variations of the $\lambda$ and $C_p$ are larger at deeper depth as shown in Table 2.

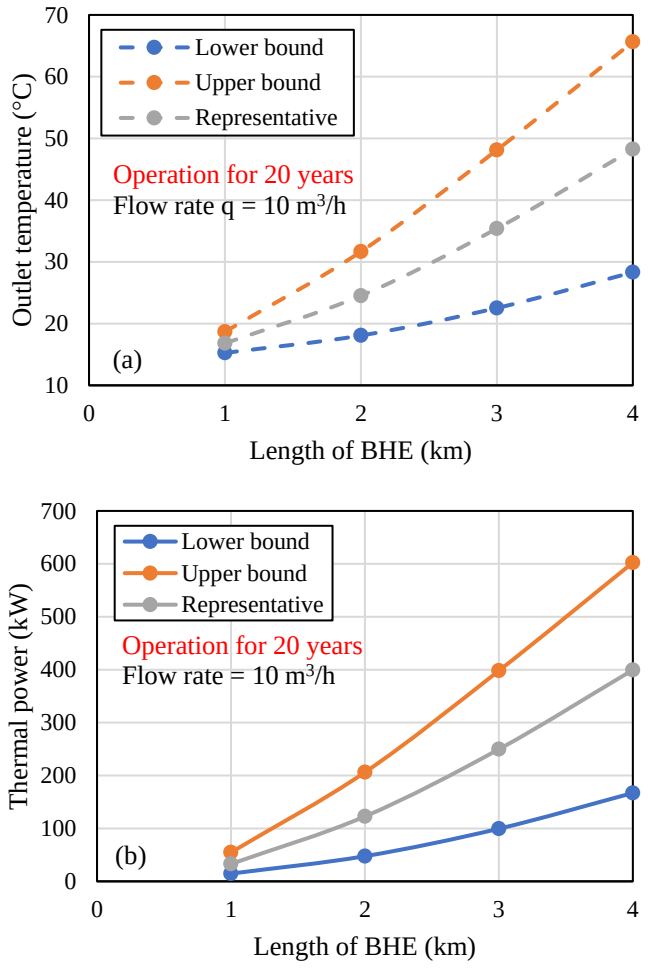


Fig. 7 Effects of formation properties on BHE after operation for 20 years at a flow rate of 10 $m^3$/h: (a) outlet fluid temperature; and (b) thermal power

## 5.2. *Effect of borehole depth*

Fig. 8 shows the effect of BHE length on the performance of BHE at different flow rates after operation for 20 years. As anticipated, the outlet temperature greatly increases with the BHE length, and the increment of outlet temperature is more obvious at the lower flow rate. Similarly, the thermal power of BHE also exponentially increases with a longer length of the BHE. However, the thermal power is larger at a larger flow rate because the thermal power is the production of flow rate and temperature differences between inlet and outlet fluid.

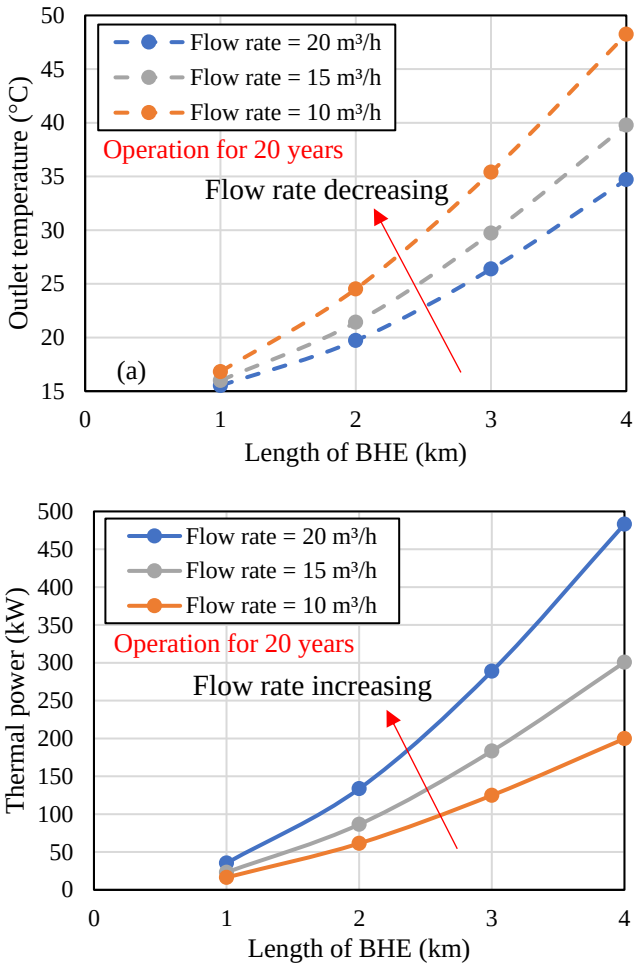


Fig. 8 Effects of borehole length on BHE after operation for 20 years at a flow rate of 10 $m^3$/h: (a) outlet fluid temperature; and (b) thermal power

## 5.3. *Effect of flow rate*

Fig. 9 plots the effect of flow rate on the performance of BHE with different lengths after operation for 20 years. At a higher flow rate, the outlet fluid temperature gradually decreases because the water has a shorter time to exchange heat with the formation. The decrease of outlet temperature with flow rate is more significant for BHE with relatively long lengths (length = 3 and 4 km). On the other hand, the thermal power of BHE increases with the flow rate because the thermal power is the production of the flow rate and temperature increment of the working fluid. And the increase in flow rate can over-compensate the decrease in outlet temperature, leading to increased thermal power. The effect of the flow rate is milder at flow rates above 15 $m^3$/h. Considering that the fluid with a higher outlet temperature can be used more easily, a trade-off could be made between the thermal power and outlet temperature. For example, a low-temperature hydronic heating system operates with fluid running between 60°F and 130°F (≈16°C and 54°C), the outlet water (48.2 °C) of the BHE with a length of 4 km and a flow rate of 10

$m^3$/h can be directly used for the system at the highest temperature setting.

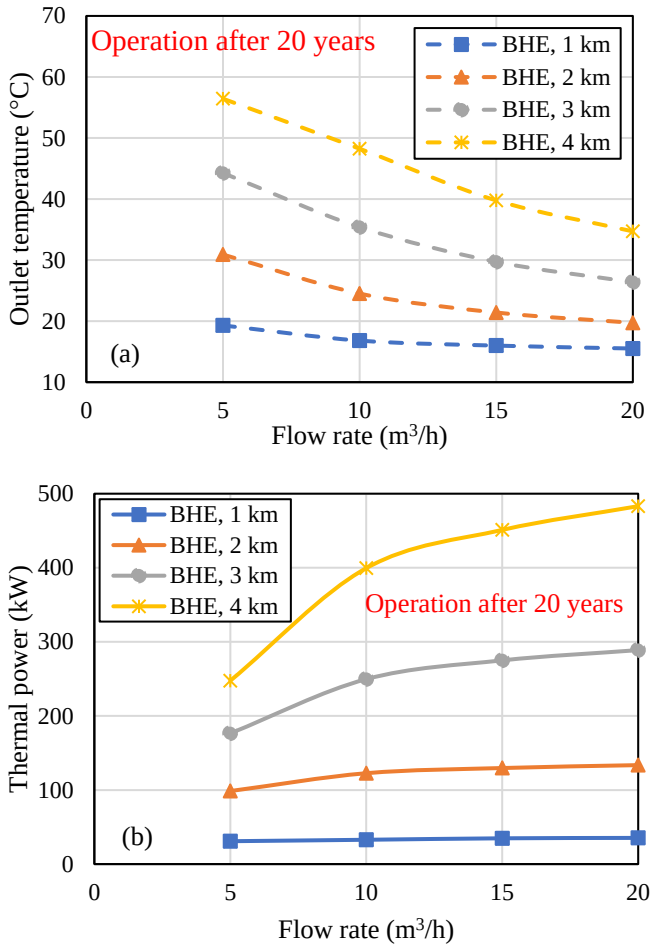


Fig. 9 Effects of flow rate on BHE after operation for 20 years: (a) outlet fluid temperature; and (b) thermal power

## CONCLUSION

This paper investigates the feasibility of the UCSD site location for installing and utilizing a BHE well. Feasibility study utilizes known geological data, data from nearby wellbores in the region, and numerical modeling. A numerical scheme for modeling Navier-Stokes fluid flow and heat flow and transport in the BHE system uses the finite element method and is adopted for modeling. The numerical model was validated with a field test on BHE available from the literature. Then the effects of the thermal properties, volumetric flow rate, and other relevant parameters were systematically analyzed by using the developed numerical modeling. The following major conclusions can be found:

1. The ground formation around the UCSD site can be generally classified into 8 layers, and the representative thermal conductivities of different layers are around 2 W/(m·K).
2. Longer length of BHE gives higher outlet fluid temperature and larger thermal power. The maximum thermal power of a 4 km-long BHE at a flow rate of 10 $m^3$/h can be 600 kW under the optimum geological parameters, whilst a thermal power of 167 kW can be obtained for the worst scenario.
3. Increasing flow rate results in lower outlet fluid temperature but higher thermal power. Considering that the fluid with a higher outlet temperature can be used more easily, a trade-off could be made between the thermal power and outlet temperature. A 4 km BHE operating at a flow rate of 10 $m^3$/h with the recommended thermal properties can produce a relatively high thermal power of 451 kW and outlet fluid temperature of 48.2°C, which can be directly used for a low-temperature hydronic heating system.

## REFERENCES


1. ANSYS, Inc. (2016) ANSYS Fluent, Release 17.2.
2. Bu, X., Ran, Y., & Zhang, D. (2019). Experimental and simulation studies of geothermal single well for building heating. *Renew. Energ.*, 143:1902–1909. https://doi.org/10.1016/j.renene.2019.06.005
3. Caulk, R. A., & Tomac, I. (2017). Reuse of abandoned oil and gas wells for geothermal energy production. *Renew. Energ.*, 112:388–397. https://doi.org/10.1016/j.renene.2017.05.042
4. COMSOL AB (2022) *COMSOL Multiphysics® v. 6.1. www.comsol.com*. Stockholm, Sweden.
5. Craig, W., & Gavin, K. (2018). *Geothermal Energy, Heat Exchange Systems and Energy Piles*. London: ICE Publishing. 41–42.
6. Dalla Santa, G., Galgaro, A., Sassi, R., Cultrera, M., Scotton, P., Mueller, J., Bertermann, D., Mendrinos, D., Pasquali, R., Perego, R., Pera, S., di Sipio, E., Cassiani, G., de Carli, M., & Bernardi, A. (2020). An updated ground thermal properties database for GSHP applications. *Geothermics*, 85:101758. https://doi.org/10.1016/j.geothermics.2019.101758
7. Diersch, H-J. G. (2014) FEFLOW finite element modelling of flow, mass and heat transport in porous and fractured media. Springer-Verlag, Heidelberg.
8. Gielen, D., Boshell, F., Saygin, D., Bazilian, M. D., Wagner, N., & Gorini, R. (2019). The role of renewable energy in the global energy transformation. *Energy Strategy Rev.*, 24:38–50. https://doi.org/10.1016/j.esr.2019.01.006
9. Gong, F., Guo, T., Sun, W., Li, Z. M., Yang, B., & Chen, Y. M. (2020). Evaluation of geothermal energy extraction in enhanced geothermal system (EGS) with multiple fracturing horizontal wells (MFHW). *Renew. Energ.*, 151:1339–1351. http://doi.org/10.1016/j.renene.2019.11.134
10. Group of Seven (G7) (2021). *G7 Industrial Decarbonisation Agenda*. London. https://assets.publishing.service.gov.uk/government/uploads/system/uploads/attachment_data/file/996388/EPD3_G7_Industrial_Decarbonisation_Agenda.pdf
11. Hartmann, A., V. Rath, & C. Clauser. (2005). Thermal Conductivity from Core and Well Log Data.

*Int. J. Rock Mech. Min. Sci.*, 42:1042–1055. https://doi.org/10.1016/j.ijrmms.2005.05.015.
12. He, Y., Jia, M., Li, X., Yang, Z., & Song, R. (2021). Performance analysis of coaxial heat exchanger and heat-carrier fluid in medium-deep geothermal energy development. *Renew. Energ.*, 168:938–959. https://doi.org/10.1016/j.renene.2020.12.109
13. Holmberg, H., Acuña, J., Næss, E., & Sønju, O. K. (2016). Thermal evaluation of coaxial deep borehole heat exchangers. *Renew. Energ.*, 97:65–76. https://doi.org/10.1016/j.renene.2016.05.048
14. Hu, X., Banks, J., Wu, L., & Liu, W. V. (2020). Numerical modeling of a coaxial borehole heat exchanger to exploit geothermal energy from abandoned petroleum wells in Hinton, Alberta. *Renew. Energ.*, 148:1110–1123. https://doi.org/10.1016/j.renene.2019.09.141
15. Iry, S., & Rafee, R. (2019). Transient numerical simulation of the coaxial borehole heat exchanger with the different diameters ratio. *Geothermics*, 77, 158–165. https://doi.org/10.1016/j.geothermics.2018.09.009
16. Kavanaugh, S. P. (1985). Simulation and experimental verification of vertical ground-coupled heat pump systems [Oklahoma State University]. https://hdl.handle.net/11244/17691
17. Kharseh, M., Al-Khawaja, M., & Hassani, F. (2019). Optimal utilization of geothermal heat from abandoned oil wells for power generation. *Appl. Therm. Eng.*, 153(5):521–535. https://doi.org/10.1016/j.renene.2021.10.038
18. Launder, B.E.; Spalding, D.B. (1974). The numerical computation of turbulent flows. *Comput. Methods Appl. Mech. Eng.*, 3 (2): 269–289.
19. Tester, J. W., Herzog, H. J., Chen, Z., Potter, R. M., & Frank, M.G. (1994). Prospects for universal geothermal energy from heat mining, *Sci. Glob. Secur.*, 5 (1):99–121. https://doi.org/10.1080/08929889408426418
20. Tester, J. W., Anderson, B., Batchelor, A., Blackwell, D., DiPippo, R., Drake, E., Garnish, J., Livesay, B., Moore, M. C., Nichols, K., Petty, S., Toksoz, N., Veatch, R., Augustine, C., Baria, R., Murphy, E., Negraru, P., Richards, M., (2006) *The future of geothermal energy: Impact of enhanced geothermal systems (EGS) on the United States in the 21st century: Massachusetts Inst. Technology*. DOE Contract DE-AC07-05ID 14517 Final Rept., 374 p.
21. United States Geological Survey (2023) San Diego Hydrogeology project. https://ca.water.usgs.gov/sandiego/wells/summary.html
22. United Nations Department of Economic and Social Affairs (UN DESA) (2017). Sustainable Development Goal 7: Ensure Access to Affordable, Reliable, Sustainable and Modern Energy for All, UN DESA, New York, NY. https://sustainabledevelopment.un.org/sdg7.
23. Wang, H. J., Xu, Y. S., Sun, Y. K., Zhao, S. M. (2022). Heat extraction by deep coaxial borehole heat exchanger for clean space heating near Beijing, China: Field test, model comparison and operation pattern evaluation. *Renew. Energ.*, 199:803–815. https://doi.org/10.1016/j.renene.2022.09.017
24. White, D. E. (1966). Geothermal energy. Bull Volcanol 29: 481–483. https://doi.org/10.1007/BF02597170